Interaction Potential Models for Bulk ZnS, ZnS Nanoparticle, and ZnS Nanoparticle-PMMA From First-Principles

Sadanandam Namsani,[a] Nisanth N. Nair,*[b] and Jayant K. Singh*[a]

An *ab initio* derived transferable polarizable force-field has been developed for Zinc sulphide (ZnS) nanoparticle (NP) and ZnS NP-PMMA nanocomposite. The structure and elastic constants of bulk ZnS using the new force-field are within a few percent of experimental observables. The new force-field show remarkable ability to reproduce structures and nucleation energies of nanoclusters (Zn_1S_1-$Zn_{12}S_{12}$) as validated with that of the density functional theory calculations. A qualitative agreement of the radial distribution functions of Zn—O, in a ZnS nanocluster-PMMA system, obtained using molecular mechanics molecular dynamics (MD) and *ab initio* MD (AIMD) simulations indicates that the ZnS–PMMA interaction through Zn—O bonding is explained satisfactorily by our force-field. © 2015 Wiley Periodicals, Inc.

DOI: 10.1002/jcc.23912

Introduction

Zinc sulphide (ZnS) has gained attention due to its wideband gap semiconductor for applications in optoelectronic devices, blue light emitting diodes, electroluminescent devices.[1,2] ZnS bulk material has a direct band gap of 3.66 eV and it is a very good phosphor host.[3,4] The band gap of ZnS increases with reduction of its size from bulk material to nanomaterial.[5,6] Thus, ZnS nanoparticles are considered to be highly promising material having numerous applications in solar cells,[7] electro-optical, and electronic devices.[8–10] ZnS can readily absorb moisture and can oxidize in air,[11] which makes ZnS less stable as pure compound in atmosphere. Hence, surfactants or capping agents are added to the nanoparticles to prevent structural transformation and surface reactions. Further, these agents prevent nanoparticles to agglomerate, which is important for maintaining the separation between nanoparticles for quantum confinement.[12] Recent biological applications of ZnS coated core-shell nanocrystals in living cell imaging[13,14] created greater interest in the study of ZnS interactions with various biomolecules. In this direction, Nawrocki and Cieplak[15] used molecular dynamics (MD) simulations to study the interactions of amino acids and small proteins with ZnS surface in water solvents. ZnS nanoparticles are optically active in the UV-visible range. However, to allow photoluminescence, surface-capping material for ZnS nanoparticles requires display of ultraviolet absorption below the absorption edge of ZnS. This strict requirement excludes most of the surfactants/polymer from the list of suitable capping agents for ZnS nanoparticle. PMMA is one of the material which satisfies the above requirement.[12]

Numerous experimental investigations on ZnS nanoparticle-polymer nanocomposites have been done. For instance, Hwang et al.[1] synthesized ZnS nanocrystals-based poly (acrylic acid) hybridized nanoparticle for polymer light emitting diodes. PMMA and Mn doped ZnS nanocomposite plaques are used as a surface cover on Si solar cell to increase the efficiency of the solar cell.[7] ZnS nanocrystals poly(urethane-methacrylate macromer) nanocomposite films with high refractive index prepared by Lü et al.[16] show high optical transparency in the visible region. Agarwal et al.[17] studied the dispersion and agglomeration behavior of ZnS nanoparticles in a PMMA matrix. Moreover, they also studied the mechanical properties of ZnS-PMMA polymer composite for various ZnS nanoparticles concentrations. Guo et al.[18] revealed that ZnS nanocrystals functionalized with the methacryloxy-propyltrimethoxysilane show high dispersion in PMMA matrix. However, the particle size of as prepared ZnS nanocrystals was found to be 2.6 nm. It was observed by the authors that the robust bonding of ZnS surface with the organic ligand made the nanoparticles stable and dispersible in PMMA matrix. Recently, Chen et al.[19] prepared poly (acrylic acid) ligand stabilized ZnS nanocrystals-polymer hybrid and reported enhanced dispersion and stabilization of grafted ZnS nanoparticles in the polymer matrix. The above experimental investigations on ZnS-PMMA nanocomposites using different polymer ligands clearly indicate that suitable interaction of nanoparticles with polymer is extremely important for its stability in polymer matrix. Hence, for practical applicability of ZnS-polymer nanocomposites a better understanding of the interactions of ZnS surface with polymer and organic ligands is required.

In ZnS, the transfer of two electrons from the metal atom to the nonmetal atom is incomplete, so that the bond between

[a] *S. Namsani, Jayant K. Singh*
Department of Chemical Engineering, Indian Institute of Technology Kanpur, Kanpur 208016, India
[b] *N. N. Nair*
Department of Chemistry, Indian Institute of Technology Kanpur, Kanpur 208016, India
E-mail: nnair@iitk.ac.in or jayantks@iitk.ac.in
Contract grant sponsor: Department of Science and Technology, Government of India

the formal Zn^{2+} and S^{2-} ions has significant covalent character.[20] Hence, model of ZnS bulk or nanoparticle should include accurate bonding and nonbonding information, which must also account for the polarizability. A shell model is typically added to the basic potential model to account for the ion polarizability for such system. Wright and Jackson[21] developed a shell model for ZnS to get the defective lattice properties of sphalerite and wurtzite by adding a massless shell to every S ion. This shell model was used by Zhang et al., in MD studies, to understand the phase stability,[22] structural transformation with water,[23,24] aggregation, coarsening and phase transformation in ZnS nanoparticles.[25] Furthermore, to explore the influence of a higher order interaction, Wright and Gale[26] refined their model for ZnS wurtzite and zincblende structures by including a three body potential with an exponential decay term and a four body potential with a tapering function. However, four-body empirical force-field is typically not in use in popular software such as DL_POLY. A few other interatomic potentials for ZnS are present in literature.[27,28] For example, Hamad et al. developed a ZnS potential[27] based on experimental data and studied the structure, properties and relative stabilities of nanoclusters of different sizes.[29–31] The empirical force-field developed by Hamad et al.[27] and Wright and Gale[26] are transferable to ZnS nanoclusters of various sizes. Similarly, two-body empirical force-field, developed by Grünwald et al.[28] for ZnS was also obtained by fitting the available experimental data, which were used only to describe the lattice and elastic constants of the bulk ZnS. However, ZnS interaction potential between ZnS clusters and a polymer or organic ligands has not been developed to our knowledge, which is essential to model the industrially important ZnS-polymer composite systems. In this direction, to understand the interactions of polymer with the surface of the nanoparticles at the atomistic level, we have developed an empirical force-field for the bulk ZnS, ZnS nanoclusters, and ZnS-PMMA composite using density functional theory (DFT). The main focus of this work is to describe the interactions between the ZnS nanoparticles and the PMMA chains, which can be used for the study of ZnS-PMMA composites using atomistic simulations.

Model and Methodology

Model for ZnS interatomic potential

It is well-known that polarization strongly affects the geometry and energetics of the molecular recognition.[32] Hence, it is very important to account for the polarizability of ions in the system. Polarizable force-fields account for appropriate changes in charge distributions. Based on the electronegativity values of S and Zn atoms S is more polarizable than Zn in ZnS.[33] Hence, we introduced polarization of S in our potential model using a polarizable core-shell model.[34] The core-shell model for S is parameterized with the constraint that the total charge of core and the shell is 2^-. For Zn ions, a fixed charge of 2^+ is used. In case of S ions, the charges of cores and shells are different, and are allowed to vary while optimizing the potential parameters. The core and the shell of a particular S ion interact through the harmonic spring, connected between them. The nonbonded van der Waals interactions between Zn core-S shell and S shell-S shell are also accounted in the potential model. However, there is no van der Waals interaction between Zn core- Zn core, Zn core-S core, and S core-S core pairs. The nonbonded interactions for Zn core–S shell and S shell–S shell are described by the Buckingham two body potential which has the form

$$U_{ij}^{\text{buck}} = A_{ij}\exp\left(-\frac{r_{ij}}{\rho_{ij}}\right) - C_{ij}r_{ij}^{-6} \quad (1)$$

where, i and j are atomic indexes (and is either a Zn or a S atom in this case), A_{ij}, ρ_{ij}, and C_{ij} are parameters. The above two-body potential alone is not adequate to maintain the internal structure of the bulk ZnS material and thus a three-body bonding potential is included. Here, we choose a harmonic three-body potential with exponential decay term[26] as shown in eq. (2). Exponential decay term in this model avoids discontinuous behavior of the potential with respect to the atom movement in the coordination shells.

$$U_{jik}^{b} = \frac{1}{2}k_\theta\left(\theta_{jik}-\theta_o\right)^2\exp\left(-\frac{r_{ij}}{\rho_1}\right)\exp\left(-\frac{r_{ik}}{\rho_2}\right) \quad (2)$$

where, k_θ, θ_0, ρ_1, and ρ_2 are parameters.

Model for PMMA–ZnS interaction potential

We have used Buckingham potential to model the Zn—O (oxygen connected to C by double bond in PMMA) and S—O (oxygen connected to C by double bond in PMMA) interactions. A three body harmonic potential is used to describe the behavior of Zn—O—C and S—Zn—O angles:

$$U_{ijk} = \frac{1}{2}k_\theta\left(\theta_{ijk}-\theta_0\right)^2 \quad (3)$$

All other intermolecular pairwise interactions, Zn—C, Zn—H, S—C, S—H, S—O (oxygen in ester group of PMMA), and Zn—O (oxygen in ester group of PMMA), between ZnS and PMMA are modeled using the 12-6 Lennard-Jones (LJ) potential:

$$U_{ij}^{\text{LJ}} = 4\epsilon_{ij}\left[\left(\frac{\sigma_{ij}}{r_{ij}}\right)^{12} - \left(\frac{\sigma_{ij}}{r_{ij}}\right)^{6}\right] \quad (4)$$

where, ε and σ are parameters. The cross interaction LJ parameters are calculated using the Lorentz–Berthelot mixing

$$\varepsilon_{ij} = \sqrt{\varepsilon_{ii}.\varepsilon_{jj}} \text{ and } \sigma_{ij} = \frac{\left(\sigma_{ii}+\sigma_{jj}\right)}{2}. \quad (5)$$

We use the derived potential parameters for ZnS and the optimized potentials for liquid simulations (OPLS) force-field parameters[35] for PMMA to describe intramolecular

Table 1. Crystal structure data of ZnS zincblende[a] and wurtzite[b] structures.

Zincblende structure parameters		
Lattice constant (Å)	5.410	
Space group	$F-43m$	
Atom	Wyckoff positions	
	Position	(x, y, z)
Zn	4a	(0,0,0)
S	4c	(1/4, 1/4, 1/4)
Wurtzite structure parameters		
Lattice constants (Å)	$a = 3.8227$, $b = 3.8227$, $c = 6.2607$	
Space group	$P63mc$	
Atom	Wyckoff positions ($u = 0.3748$)	
	Position	(x, y, z)
Zn	2b	(1/3,2/3,0) (2/3,1/3,1/2)
S	2a	(1/3,2/3,u) (2/3,1/3,u+1/2)

[a] Birman et al.[39] [b] Kisi et al.[40]

interactions. For all the nonbonded interactions, a cutoff of 12 Å is used.

Method for evaluation for potential parameters

Interaction potentials for ZnS and PMMA–ZnS systems are derived by fitting to various reference structures and corresponding total energies, computed using DFT. In this study, the reference energies are obtained using DFT calculations performed using plane-wave (PW) basis set. To derive the force-field parameters, we optimize the parameters until the calculated and the reference energies are as close as possible. This fitting procedure is performed using the GULP program,[36–38] where the force-field parameters are optimized by minimizing the function

$$F = \sum_{i=1}^{N_{obs}} w_i \left(f_i^{obs} - f_i^{calc} \right)^2 \quad (6)$$

where N_{obs} is the number of observables, F is the sum of squares, f_i^{calc} and f_i^{obs} are the calculated and the observed values, and w_i is a weighting factor. The minimization converges if gradients on all the optimization variables (i.e., the force-field parameters) are below a defined convergence of 0.0001 eV/Å.

The observables used in fitting of the potential parameters for ZnS bulk system are energy-volume data generated from PW DFT calculations. Conversely, the observables for fitting of PMMA–ZnS potential parameters are coordinates and the corresponding total energy obtained by changing Zn—O bond length, S—Zn—O, and Zn—O—C angles using PW DFT calculations. Technical details of the DFT calculations are described in a later section.

(a) Observables for ZnS Bulk Structures

It is crucial to have the structure and mechanical properties of the ZnS in different phases being reproduced accurately using the derived ZnS parameterized potential. Therefore, we have chosen bulk energy of ZnS in zincblende and wurtzite phases as observables for different values of the cell volume. For these reference calculations, a 3 × 3 × 3 supercells, as generated from the crystallographic data of the zincblende[39] and wurtzite structures (see Table 1)[40] are used. The generated 3 × 3 × 3 supercells of zincblende ($Zn_{108}S_{108}$) and wurtzite ($Zn_{54}S_{54}$) structures are shown in Figures 1a and 2b, respectively. Cartesian coordinates of $Zn_{108}S_{108}$ and $Zn_{54}S_{54}$ in the 3 × 3 × 3 supercells are generated for different supercell volumes, that is, by changing the unit cell parameters, about the experimental value, while preserving the bulk symmetry of ZnS. The energy for these structures are then computed using PW DFT, and the resulting energy-volume data is fitted to the Birch–Murnaghan equation[41] (Birch EOS) to get the equilibrium volume, unit cell parameters, and bulk modulus.

(b) Observables for PMMA–ZnS system

To generate the observables for fitting of interaction model for PMMA–ZnS, we first used a system of three-monomer chain of PMMA ($n = 3$; see Fig. 2) bound to Zn_6S_6 cluster system. The optimized structure (In this work, structural optimizations are carried out for this system at the DFT/PBE/6–31G** level employing the Gaussian09 program; see Supporting Information for the full reference of Gaussian09.) of this system is shown in Figure 3, where it is evident that the carbonyl oxygens (C═O) of PMMA is bonded with two Zn atoms of the Zn_6S_6 cluster.

Various structures of this system are generated by changing the Zn—O bond length, Zn—O—C, and S—Zn—O bond angles about their equilibrium values. The structure and total energy data as obtained by PW DFT calculations are used to derive the force-field parameters for the PMMA–ZnS interactions.

(c) PW DFT calculations

All the PW DFT calculations, including the *ab initio* MD (AIMD) simulations, are performed using the PBE density functional and Ultrasoft psuedopotentials[42] as implemented in the CPMD code.[43,44] A PW cutoff of 25 Ry is used. All the calculations are performed at the gamma point. Wavefunction optimization is performed till the wavefunction gradient is converged to 10^{-7} a.u.

In addition, for modeling the isolated PMMA-Zn_6S_6 cluster with 3 PMMA repeat units and other bare ZnS clusters, the Hockney Poisson[45] solver is used with a cubic supercell of 40 and 35 Å box lengths, respectively, unless otherwise specified. In these calculations, a vacuum gap of about 12 Å is present between the periodic images. For PMMA-Zn_6S_6 cluster system with 20 PMMA chains of 3 repeat units, a periodic box of size of 21.93 Å is used.

(d) MM MD simulations

All the molecular mechanics molecular dynamics (MM MD) simulations using the derived force-field are performed at a temperature of 300 K using the DL_POLY code[46] with a nonbonding interaction cutoff of 12 Å. An extended Lagrangian core-shell dynamics has been performed, where shell variables are given a mass of 0.2 a.u. and a timestep of integration of 0.5 fs is used. We used Nosé–Hoover barostat[47] for NPT (constant number (N), constant pressure (P), and constant temperature (T)) variable cell MD simulations and Nosé–Hoover[48] thermostat in NVT (constant number (N), constant volume (V), and constant temperature (T)) MD simulations.

To generate the normalized probability distributions of Zn—O bond, Zn—O—C, and S—Zn—O angles in the PMMA-Zn_6S_6

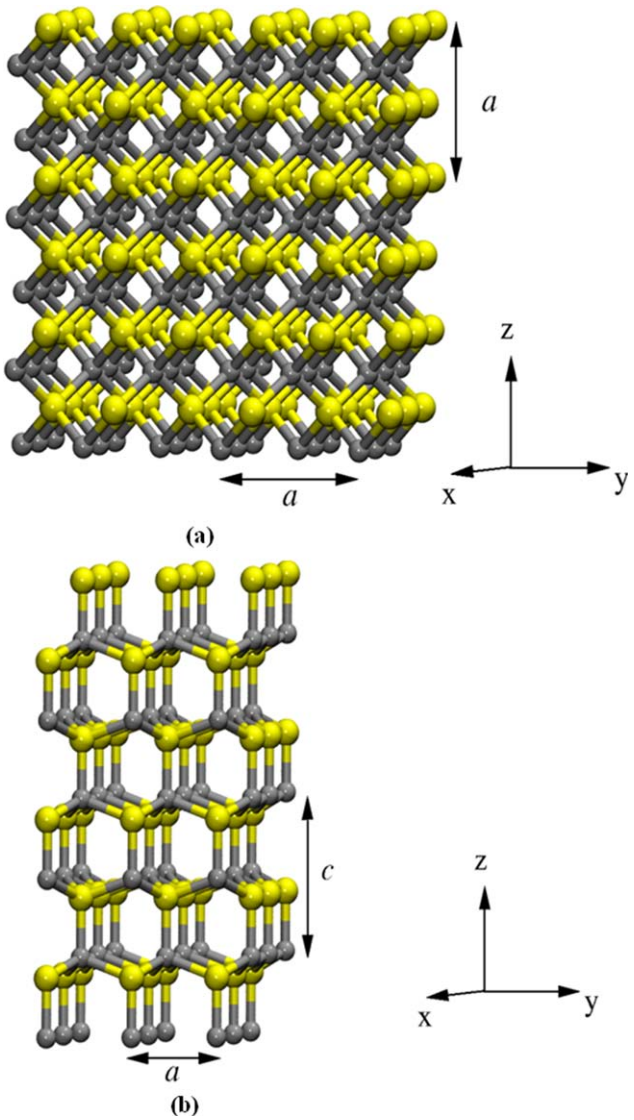

Figure 1. a) ZnS supercell of 3 × 3 × 3 zincblende structure consisting of $Zn_{108}S_{108}$; dark gray (Zn) and yellow (S). b) ZnS supercell of 3 × 3 × 3 wurtzite structure consisting of $Zn_{54}S_{54}$; dark gray (Zn) and yellow (S).

system containing 3 PMMA repeat units, NVT MD simulation runs are performed at 300 K using 2 ns equilibration followed by 1 ns production run. To exclude periodic image interactions, a cubic supercell of box length 60 Å is used. Further, to test the force-field on a large system, we performed NPT MD simulations of the PMMA-Zn_6S_6 system containing 20 chains of 3 PMMA repeat units at 300 K and 1 atm. A 3 ns NPT simulation is performed followed by a 1 ns NVT simulation using the equilibrated cell. The NVT trajectory is used to compute radial distribution function (RDF) for Zn—O.

(e) AIMD simulations

All AIMD simulations are performed using the Car–Parrinello approach[49] using the CPMD code.[43,44] Timestep of 0.145 fs is used to integrate the equation of motion during the dynamics. A fictitious orbital mass of 700 a.u., Nosé–Hoover chain thermostats[50] is used to control the kinetic energy of the fictitious dynamics of orbitals and to obtain canonical ensemble for nuclear degrees of freedom at 300 K.

NVT AIMD simulations of PMMA-Zn_6S_6 system containing 1 and 20 PMMA chains of 3 repeat units are performed for 150 and 34 ps, respectively.

Results and Discussions

Structural properties of bulk ZnS and ZnS nano clusters

For zincblende structure of ZnS, the fitting of the energy-volume curve generated using the DFT calculations with the Birch EOS is shown in Figure 4. The computed equilibrium cell parameter for zincblende structure is in good agreement with the experimental data,[51] with less than 1% error, and even outperforms the results of Jaffe et al.[52] and Qteish and Parrinello[53] obtained using HF-LCAO method and pseudopotential method, respectively. In addition, the value of the cell parameter obtained in this work is also in good agreement with the Perdew-Wang 1991 generalized gradient approximation and TB-LMTO method reported data of Chen et al.[54] and Gangadharan et al.,[55] respectively. Furthermore, the calculated bulk modulus value is 69.04 GPa, which is in agreement with the available experimental data[51] and other theoretical calculations.[35,52,55] Table 2 summarizes the DFT-based zincblende structural data and corresponding literature data.

Similar to the zincblende ZnS, Figure 5 shows the fitting of the Birch EOS for the wurtzite structure. The computed cell parameters are in good agreement, within 1% of the experimental data[26] and other theoretical calculations.[56–58] The bulk modulus obtained from the fit is 69.25 GPa, which is in good agreement with the previous DFT calculation,[58] and also agrees well with the experimental value[26] of 74.00 GPa. The comparison between computed wurtzite structure data and literature is shown in Table 2.

Energy-volume data obtained for zincblende and wurtzite are then used to obtain the ZnS potential parameters. The derived potential parameters are tabulated in Table 3.

To assess the quality of the new force-field, we calculate first the structural parameters of zincblende phase, using the new force-field, which are summarized in Table 4. Here, C_{11}, C_{12}, and C_{44} are elastic constants, which relate stress and strain in a linear fashion. The elastic constants are defined as the second derivative of the energy density with respect to strain.[37,62] The optimized cell parameter for zincblende is 5.419 Å, which is in very good agreement with the experimental data. The new force-field overestimates the cell parameter by only 0.17% with respect to the experimental value.[51] Interestingly, this result is better than the previous theoretical calculations. For example, Jaffe et al.[52] using HF-LCAO method overestimates the cell parameter of zincblende by 3.1%. The results of Yeh et al.,[57] Casali and Christensen,[60] and Martins et al.[63] using different methods for zincblende are consistent in getting the lattice constant of 5.345 ± 0.1 Å, which is lower than the experimental value by 1.2%.

Test calculations are also done for the ZnS wurtzite structure, using the new force-field (Table 5). The obtained cell parameters of the wurtzite structure, *a* and *c* are 3.876 and 6.141 Å, respectively. The cell parameters, *a* and *c* deviate from the experimental values by 0.67 and 2.37%, respectively.

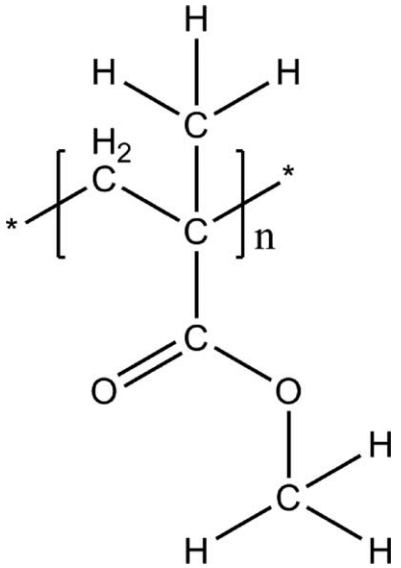

Figure 2. PMMA repeat unit chemical structure.

LAPW method-based results of Yeh et al.[57] are 3.777 and 6.188 Å, which are lower than the experimental wurtzite cell parameters *a* and *c* by 1.9 and 1.6%, respectively. The DFT calculations of Catti et al.[56] over predicts both the cell parameters *a* and *c* by 3.3%. This shows that the results of the newly derived force-field are in good agreement with the experimental values and outperforms the data reported by Catti et al.[56]

The performance of the new force-field is comparable to that of the existing interatomic potentials[26,27] (see Table 5). The bulk modulus values of zincblende and wurtzite are also well reproduced, and the errors when compared with experimental values are 3.65 and 1.3%, respectively. The bulk modulus values calculated using the derived potentials in this work are in agreement with the existing potential model of Wright and Gale[26] and outperforms the results of Hamad et al.[27]

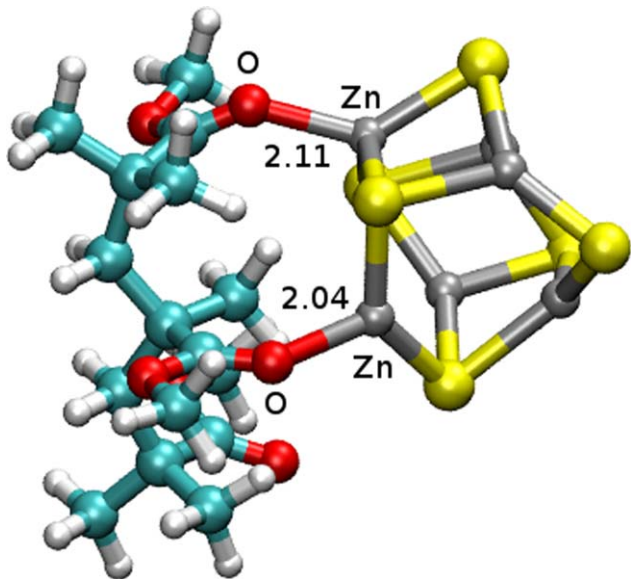

Figure 3. DFT optimized structure of PMMA with Zn_6S_6 cluster; red oxygen (O), dark gray (Zn), and yellow (S).

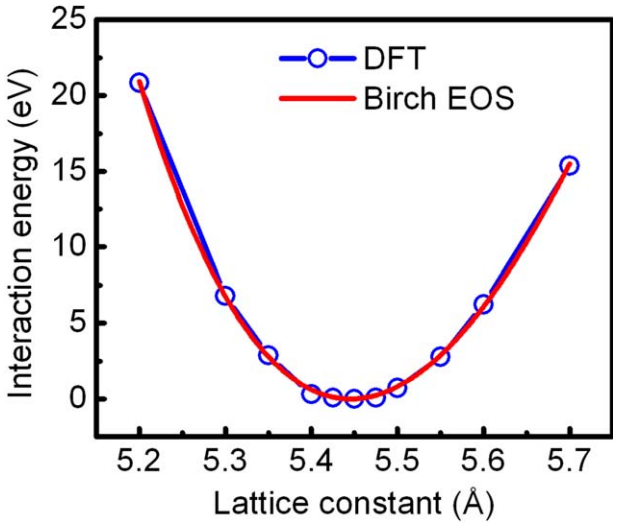

Figure 4. Energy-volume data generated using DFT for 3 × 3 × 3 for ZnS zincblende structure. The solid red curve represents the fit to the Birch–Murnaghan equation. [Color figure can be viewed in the online issue, which is available at wileyonlinelibrary.com.]

The experimental elastic constants of zincblende structure are significant scattered in values. C_{11}, C_{12}, and C_{44} elastic constant values are in the range: 94.2–104.5, 56.8–65.3, and 34–46 GPa, respectively.[26] The elastic constants using the new force-field, falls in the aforementioned range. The C_{11} value of zincblende structure is well reproduced, and the error is 0.04% when compared with the experimental data.[52] In our study, the C_{12} values are considerably underestimated but the values are in agreement with the Wright and Gale[26] reported values and other theoretical calculations.[54,61] Similarly, C_{44} values are in line with the previous empirical force-field[26,27] reported values. However, they are considerably lower than the experimental data. Our force-field estimated dielectric constants are in good agreement with the experimental data[26] (error less than 1.2%) and the agreement is better than that by the empirical force-field of Wright and Gale.[26] The elastic constant C_{44} of wurtzite is considerably under estimated when compared with the experimental and previous theoretical values.[26] Other elastic constants of wurtzite are in good agreement with that of previous studies.[26]

Furthermore, to test the ZnS force-field parameters, the optimized empirical force-field parameters are used to obtain the energy-volume data of zincblende structure and wurtzite structure by varying the lattice parameters around its experimental values. These results are also compared with the periodic DFT calculations. The energy-volume data obtained using our force-field is in good agreement with that from DFT computations as clearly evident from Figures 6a and 6b.

Although the new empirical force-field is trained using the bulk data as obtained from DFT, the force-field is transferable to small clusters. Figure 7 presents the optimized structures obtained using the derived force-field. These structures are in good agreement with the DFT optimized structures. The bond lengths and angles of these clusters are in good agreement, within 0.1 Å and 2° variations, respectively, with the DFT optimized structures.

Table 2. Comparison of the DFT computed unit cell parameters and bulk modulus for the ZnS zincblende and wurtzite structures with experimental and literature data.

Zincblende structure data			
Parameter	Present work	Experimental data[52]	Literature data
Lattice constant (Å)	5.446	5.410	5.580,[a] 5.352,[b] 5.404,[c] 5.400[d]
Bulk modulus (GPa)	69.04	76.90	75.90,[a] 83.10,[b] 71.22,[c] 80.97[d]
Wurtzite structure data			
Parameter	Present work	Experimental data[26]	Literature data
Lattice constant (*a*, Å)	3.862	3.850	3.982,[d] 3.777,[e] 3.840[f]
Lattice constant (*c*, Å)	6.224	6.290	6.500,[d] 6.188,[e] 6.267[f]
Bulk modulus (GPa)	69.247	74.000	68.960,[f] 68.519[g]

[a] Jaffe et al.[52] [b] Qteish and Parrinello.[53] [c] Chen et al.[54] [d] Gangadharan et al.[55] [e] Catti et al.[56] [f] Yeh et al.[57] [g] Hu Cui et al.[58]

To further verify the transferability of the new force-field, we calculate the nucleation energies of these clusters. Figure 8 presents the force-field-based nucleation energies along with that from the PW DFT. The nucleation energies of a cluster, $(ZnS)_n$, is defined as

$$E_{nuc}(n) = E(n) - E(n-1) - E_{ZnS}^{bulk} \quad (7)$$

where $E(n)$ is the total energy of $(ZnS)_n$ cluster and E_{ZnS}^{bulk} is the energy per ZnS unit in the bulk zincblende structure. The computed nucleation energies of these clusters using the derived empirical force-field are compared with the DFT results.

The force-field based nucleation energies are in good agreement with our DFT calculations, which is clearly evident in Figure 8. The comparison is superior for larger cluster. Based on this, it can be inferred that the new empirical force-field of ZnS can be used to model ZnS nanoclusters.

Structure and bonding information of PMMA and ZnS

Now, we turn our attention to the development of the intermolecular interaction parameters for the PMMA and ZnS system. This is achieved by fitting the empirical force-field parameters to reproduce the DFT structure-energy data of PMMA-Zn_6S_6 system with 3 PMMA repeat units. The optimized PMMA–ZnS interaction parameters as in eqs. (3) and (4) are shown in Table 6.

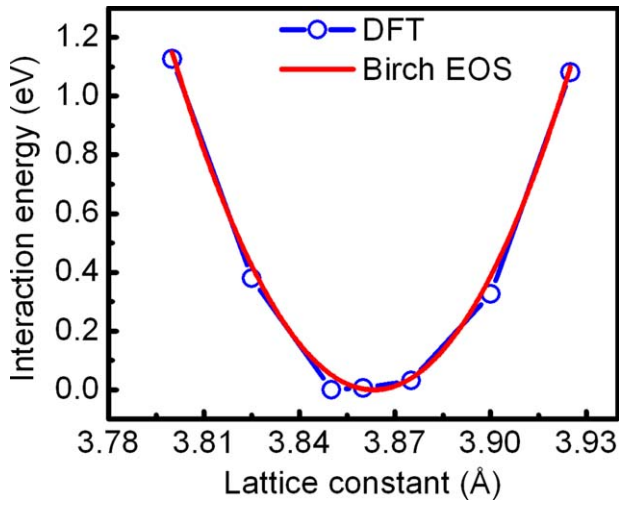

Figure 5. Energy-volume data obtained using DFT for 3 × 3 × 3 of ZnS wurtzite structure. The solid red curve represents the fit to the Birch–Murnaghan equation. [Color figure can be viewed in the online issue, which is available at wileyonlinelibrary.com.]

To demonstrate the performance of the force-field, the potential energy curves as a function of Zn—O distance computed using DFT and the new empirical potential are shown in Figure 9. Overall, the empirical force-field reproduces the DFT Zn—O potential energy curve satisfactorily. The comparison of the Zn—O—C and S—Zn—O angle bending curves generated using the force-field and DFT calculations are shown in Figures 10a and 10b, respectively. These figures indicate that the newly developed PMMA–ZnS empirical force-field could very well reproduce the angle bending motions.

Furthermore, to verify the bond and angle distributions in typical MD simulations, we perform MD simulations of one PMMA chain containing three monomers with Zn_6S_6 cluster, using DFT and the newly generated empirical force-field. The trajectories obtained from these MD simulations are analyzed to get the normalized probability distribution of Zn—O bond, Zn—O—C, and S—Zn—O angles. The Zn—O bond distribution

Table 3. ZnS potential parameters obtained using the energy-volume data of the zincblende and wurtzite structures.

Buckingham potential	*A*(eV)	*ρ*(Å)	*C*(eV/Å6)	Cutoff (Å)
Zn core–S shell	580.84615	0.400505	0.00	12.0
S shell–S shell	1199.78975	0.148604	0.00	12.0
Three-body potential	*K*(eV/rad^2)	θ_o(°)	ρ_1/ρ_2 (Å)	Cut-off (Å)
S shell-Zn core–S shell	7000859.729	109.47	0.3/0.3	12.0
Charges on ions				
Ion	Charge (*e*)			
Zn	2.0			
S core	1.087526			
S shell	−3.087526			
Spring constant				
Bond	K_s(eV)			
S core–S shell	14.380739			

Table 4. Comparison of computed lattice constant, mechanical, and elastic properties of zincblende structure using the new force-field with experimental and literature data. C_{11}, C_{12}, and C_{44} are elastic constants. ε_{11}^{0} and $\varepsilon_{11}^{\infty}$ are the static and high frequency dielectric constants.

Observable	Present work	Experimental data[26]	Literature data
Lattice constant (a, Å)	5.419	5.410[a]	5.580,[d] 5.404,[e] 5.450,[c] 5.410[h]
Bulk Modulus (GPa)	74.1	76.9[a]	75.60,[c] 80.975,[f] 71.22,[e] 80.0[h]
C_{11} (GPa)	104.05	104.00[b]	107.70,[c] 123.70,[g] 99.60,[e] 105.10[h]
C_{12} (GPa)	59.12	65.00[b]	59.40,[c] 57.00,[e] 62.01,[g] 53.55,[i] 65.30[h]
C_{44} (GPa)	26.0	46.2[b]	33.2,[c] 50.5,[e] 59.7,[g] 43.1[h]
ε_{11}^{0}	8.27	8.37[c]	6.49,[c] 6.30[h]
$\varepsilon_{11}^{\infty}$	5.20	5.20[c]	4.76[c]

[a] Modelung et al.[51] [b] Berlincourt et al.[59] [c] Wright and Gale.[26] [d] Jaffe et al.[52] [e] Chen et al.[54] [f] Gangadharan et al.[55] [g] Casali and Christensen.[60] [h] Hamad et al.[27] [i] Anil et al.[61]

obtained from empirical force-field MD is compared with the distribution obtained from AIMD simulation. The normalized probability distribution of Zn—O bond using the empirical force field is in very good agreement with the DFT calculations, which is shown in Figure 11a. The probability density distributions obtained using DFT and new force-field show maximum at 2.10 and 2.13 Å, respectively. The normalized probability distribution of Zn—O—C angle is shown in Figure 11b. The peak value of Zn—O—C angle distribution from the new force-field is 150°, which is comparable with the value, 149°, from the DFT calculations. As shown in Figure 11c the peak values of S—Zn—O angle distributions are 105.5° and 107.4° for DFT and the derived empirical force-field, respectively, which shows again a reasonable agreement with the DFT data. However, the widths of these distributions are not well captured by the force-field. We believe that this discrepancy is mainly attributed to the varying charge transfer between Zn and S during the dynamics, and thus not reflected in the empirical force-field. However, due to the difference in the width in the distributions, we may conclude that the dynamic properties of this system, in particular, the vibrational frequencies of Zn—O bonds between PMMA and ZnS are not well reproduced.

Table 5. Comparison of computed lattice constants, mechanical, and elastic properties of wurtzite structure using the new force-field with experimental and literature data. C_{11}, C_{12}, C_{44}, C_{13}, and C_{33} are elastic constants. ε_{11}^{0}, ε_{33}^{0}, and $\varepsilon_{11}^{\infty}$, $\varepsilon_{33}^{\infty}$ are the static and high frequency dielectric constants, respectively.

Observable	Present work	Experimental data[26]	Literature data
Lattice constant (a, Å)	3.876	3.850	3.982,[a] 3.777,[b] 3.840[c]
Lattice constant (c, Å)	6.141	6.290	6.50,[a] 6.188,[b] 6.267[c]
Bulk modulus (GPa)	74.96	74.0	68.96,[c] 76.4[d]
C_{11} (GPa)	102.249	122.0	118,[a] 111.3,[d] 124.2[e]
C_{12} (GPa)	58.242	58.0	52,[a] 55.6,[d] 59.8[e]
C_{44} (GPa)	35.69	28.7	31,[a] 37.7,[d] 37.3[e]
C_{13} (GPa)	60.50	42.0	39,[a] 57.9,[d] 58[e]
C_{33} (GPa)	114.61	138.0	135,[a]126.4,[d] 113[e]
ε_{11}^{0}	7.27		6.71[d]
ε_{33}^{0}	7.88		6.90[d]
$\varepsilon_{11}^{\infty}$	4.93		4.79[d]
$\varepsilon_{33}^{\infty}$	5.12		4.91[d]

[a] Catti et al.[56] [b] Yeh et al.[57] [c] Hu Cui et al.[58] [d] Wright and Gale.[26] [e] Hamad et al.[27]

Now, we turn our attention to simulate a larger PMMA-Zn_6S_6 system using the empirical force-field. To this end, we consider a system of one Zn_6S_6 cluster and 20 PMMA chains of three monomer units, and performed AIMD and MM MD

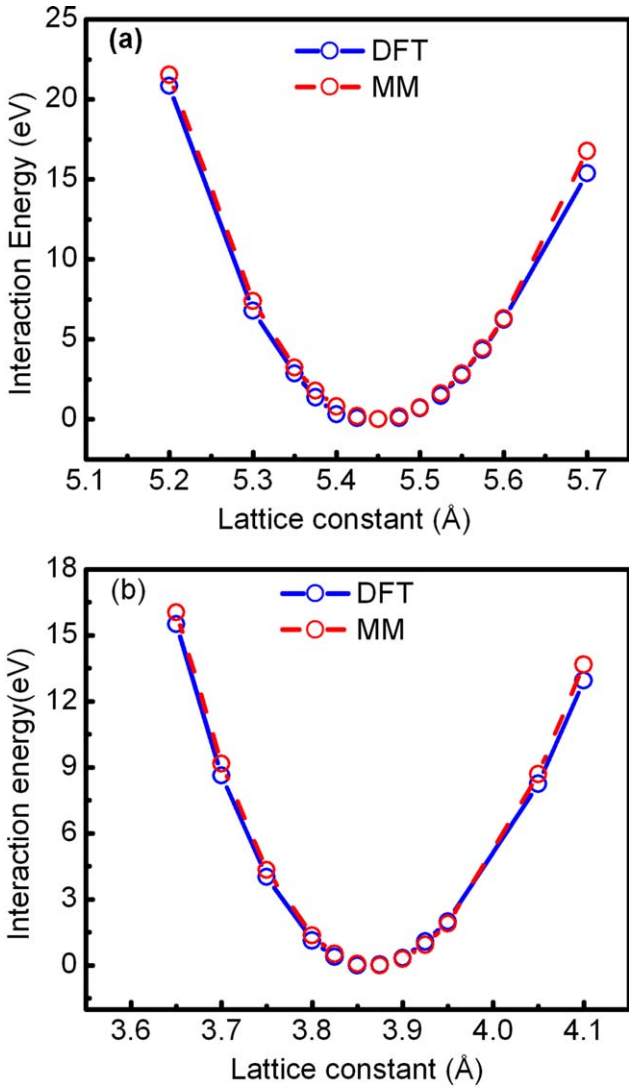

Figure 6. A comparison of energy-volume curves obtained from DFT and the new empirical force-field: a) zincblende and b) wurtzite. [Color figure can be viewed in the online issue, which is available at wileyonlinelibrary.com.]

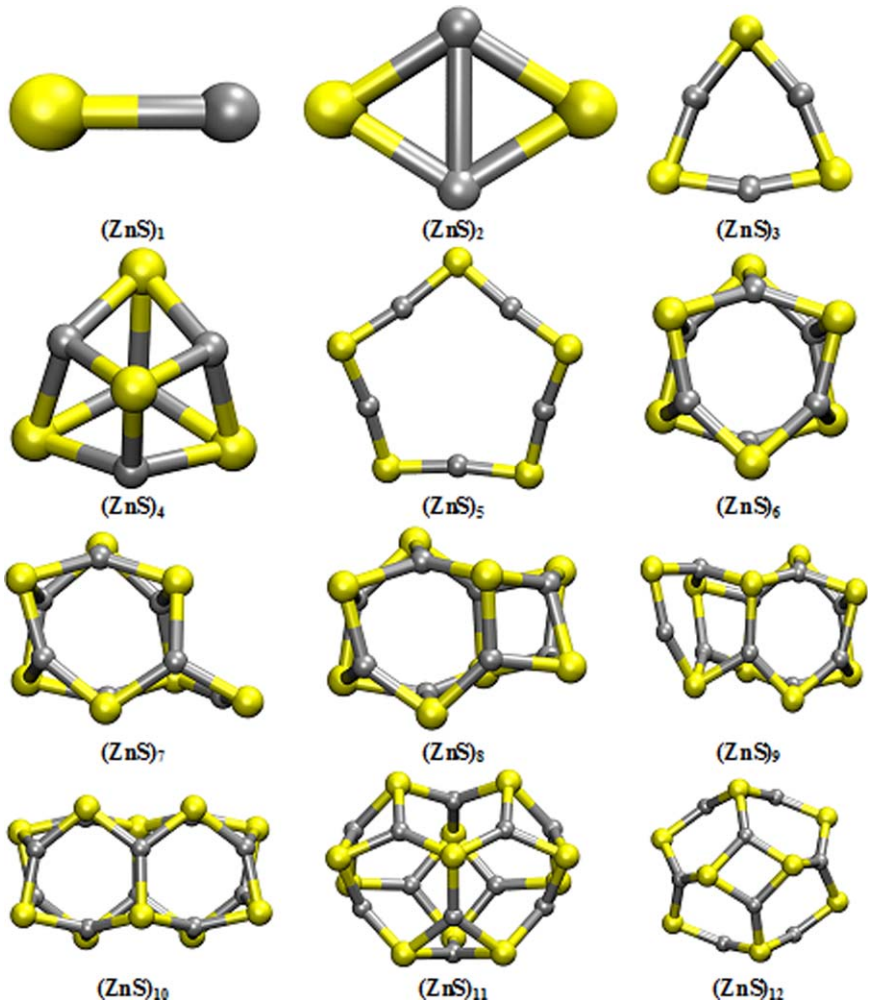

Figure 7. Optimized structures of $(ZnS)_1$–$(ZnS)_{12}$ nanoclusters using the new empirical force-field. [Color figure can be viewed in the online issue, which is available at wileyonlinelibrary.com.]

simulations to obtain the pair distributions. The RDFs for Zn—O obtained from MM MD and AIMD simulations are in good agreement as shown in Figure 12.

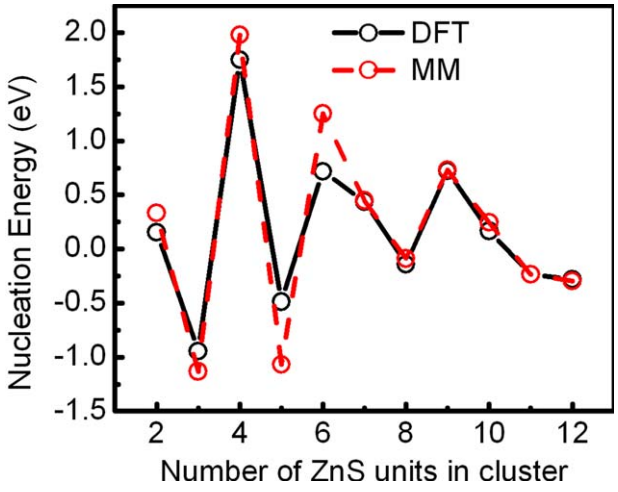

Figure 8. Comparison of nucleation energies of ZnS nanoclusters obtained from the new force-field and DFT. [Color figure can be viewed in the online issue, which is available at wileyonlinelibrary.com.]

In PMMA and ZnS system, PMMA chains interact mainly with Zn sites of nanoclusters through Zn—O bonding. The first peak at 2.15 Å in RDF of MM MD shows that there is a coordination shell of carbonyl oxygen of PMMA around the nanocluster as a result of the Zn—O coordination. This peak value is in good agreement with the average value of 2.11 ± 0.31 Å from the RDF of AIMD simulation. Coordination of carbonyl oxygen of PMMA with Zn sites was also observed by Gallagher et al.[12] in their FTIR measurements of PMMA and ZnS nanocomposite.

Table 6. Derived PMMA and ZnS interaction parameters.

Buckingham potential	A(eV)	ρ(Å)	C(eV/Å^6)	Cutoff (Å)
Zn—O (core–core)	8611.6262	0.2398	187.7828	12
S—O (shell–core)	115604.4671	0.2767	0.000	12
Three-body potential	K(eV/rad^2)		θ_o(°)	
S—Zn—O	4.5123		105.5	
Zn—O—C	3.7793		150.0	
12-6 LJ	ε(eV)		σ(Å)	
Zn	0.0009545		3.816204	
S	0.011269		4.270186	

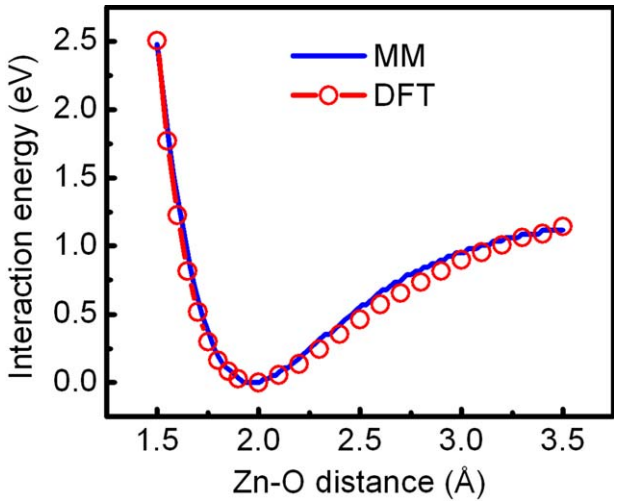

Figure 9. Comparison of normalized Zn—O bond stretching curve for PMMA-Zn_6S_6 system using the new empirical force-field and DFT. [Color figure can be viewed in the online issue, which is available at wileyonlinelibrary.com.]

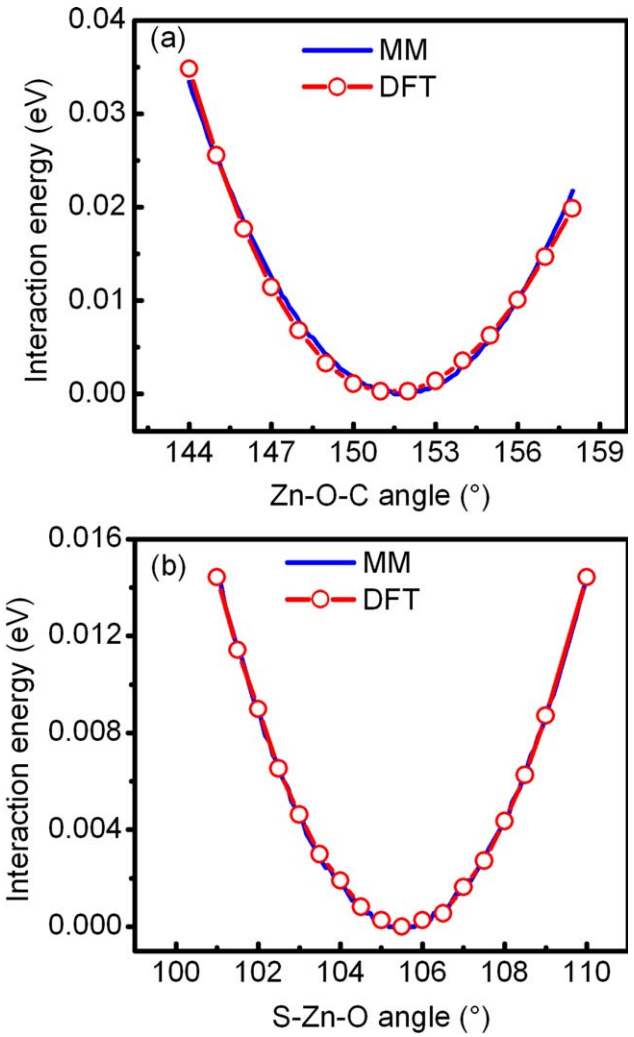

Figure 10. Comparison of normalized angle bending curves of a) Zn—O—C angle and b) S—Zn—O angle for PMMA-Zn_6S_6 system using the new force-field and DFT. [Color figure can be viewed in the online issue, which is available at wileyonlinelibrary.com.]

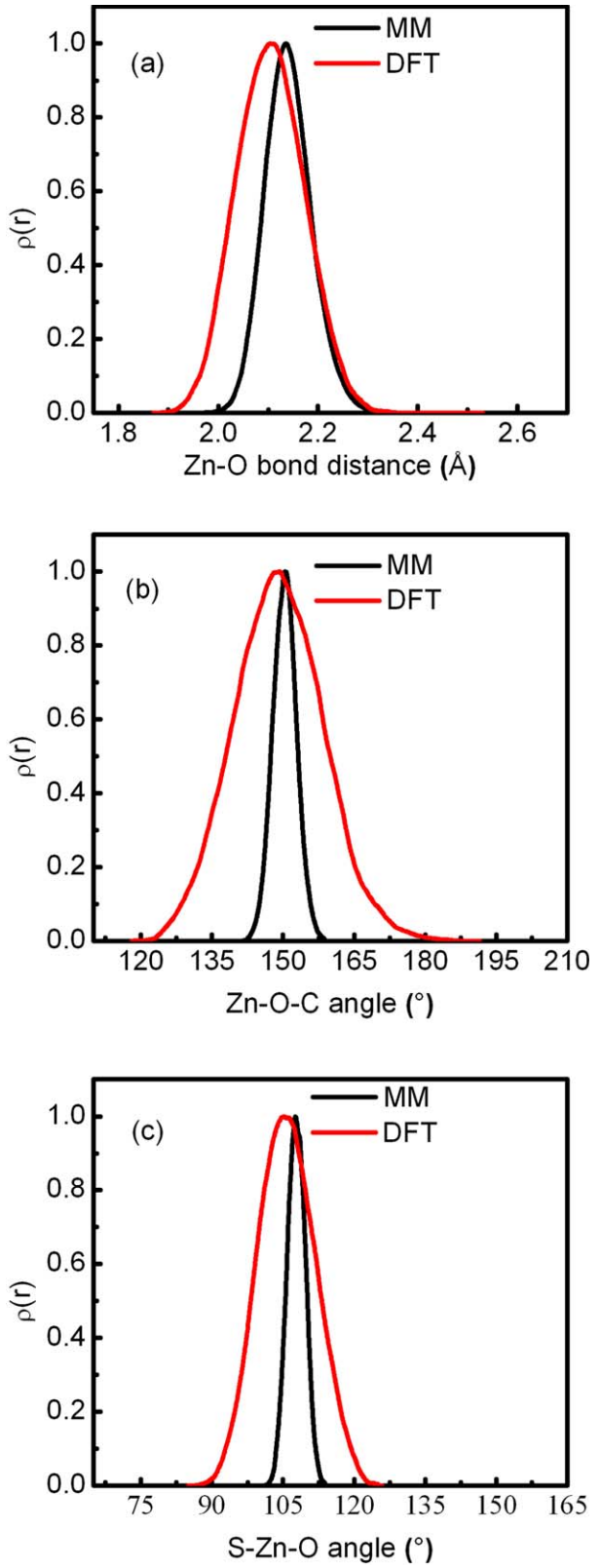

Figure 11. Comparison of the normalized probability distributions for PMMA-Zn_6S_6 from the new empirical force-field and DFT-based MD simulations: a) Zn—O bond, b) Zn—O—C angle, and c) S—Zn—O angle. [Color figure can be viewed in the online issue, which is available at wileyonlinelibrary.com.]

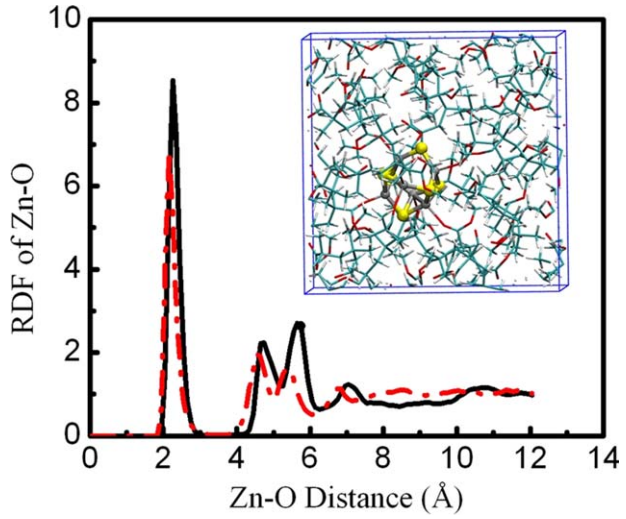

Figure 12. RDFs of Zn—O for PMMA-Zn_6S_6 system (with 20 PMMA chains of 3 repeat units, and 1 Zn_6S_6 cluster) from MD simulations: MM MD (solid black line) and AIMD calculations (dotted red line). The inset shows the equilibrated structure of the system obtained from the MM MD simulation. [Color figure can be viewed in the online issue, which is available at wileyonlinelibrary.com.]

Conclusions

In this work, we have developed an empirical force-field for the bulk ZnS, which is able to reproduce experimental structure and properties of zincblende and wurtzite phases. The force-field is found to be transferable to nanoclusters, which is checked against the DFT generated structures and energy data. Hence, this MM force-field is suitable for modeling ZnS bulk and ZnS nanoparticles. We have also reported an empirical potential for modeling PMMA and ZnS interactions. The performance of this potential is benchmarked for Zn_6S_6 cluster and PMMA systems using MD simulations. Structural parameters are reasonably well reproduced, especially the formation of Zn—O coordination. However, dynamic properties of this system, in particular, the vibrational frequencies of Zn—O bonds between PMMA and ZnS, are not well reproduced. The developed empirical force-fields are thus useful for modeling large ZnS nanoparticles dispersed in PMMA polymer matrix and for studying the structural and agglomeration behavior of nanoparticles.

Acknowledgments

The High Performance Computing (HPC) facility of Indian Institute of Technology Kanpur is gratefully acknowledged.

Keywords: ZnS · PMMA · empirical force-field · density functional theory

How to cite this article: Namsani S, Nair NN, Singh JK. *J. Comput. Chem.* **2015**, *36*, 1176–1186. DOI: 10.1002/jcc.23912

[1] J.-M. Hwang, M.-O. Oh, I. Kim, J.-K. Lee, C.-S. Ha, *Curr. Appl. Phys.* **2005**, *5*, 31.
[2] R. H. Friend, *Pure Appl. Chem.* **2001**, *73*, 425.
[3] R. N. Bhargava, D. Gallagher, X. Hong, A. Nurmikko, *Phys. Rev. Lett.* **1994**, *72*, 416.
[4] R. N. Bhargava, D. Gallagher, T. Welker, *J. Lumin.* **1994**, *60* and 61, 275.
[5] R. Maity, U. N. Maiti, M. K. Mitra, K. K. Chattopadhyay, *Physica E Low Dimens. Syst. Nanostruct.* **2006**, *33*, 104.
[6] P. K. Ghosh, S. Jana, S. Nandy, K. K. Chattopadhyay, *Mater. Res. Bull.* **2007**, *42*, 505.
[7] M. Dai Prè, I. Morrow, D. J. Martin, M. Mos, A. Del Negro, S. Padovani, A. Martucci, *Mater. Chem. Phys.* **2013**, *139*, 531.
[8] M. Matsuoka, K. I. Ono, *J. Vac. Sci. Technol., A* **1989**, *7*, 2975.
[9] M. A. Haase, H. Cheng, D. K. Misemer, T. A. Strand, J. M. DePuydt, *Appl. Phys. Lett.* **1991**, *59*, 3228.
[10] M. J. Weber, Handbook of Laser Science and Technology; CRC: Cleveland, **1986**.
[11] W. Hertl, *Langmuir* **1988**, *4*, 594.
[12] D. Gallagher, W. E. Heady, J. M. Racz, R. N. Bhargava, *J. Mater. Res.* **1995**, *10*, 870.
[13] X. Zhang, S. Mohandessi, L. W. Miller, P. T. Snee, *Chem. Commun.* **2011**, *47*, 3532.
[14] F. Chen, D. Gerion, *Nano Lett.* **2004**, *4*, 1827.
[15] G. Nawrocki, M. Cieplak, *J. Chem. Phys.* **2014**, *140*, 095101.
[16] C. Lü, Z. Cui, Y. Wang, Z. Li, C. Guan, B. Yang, J. Shen, *J. Mater. Chem.* **2003**, *13*, 2189.
[17] S. Agarwal, D. Patidar, N. S. Saxena, *J. Appl. Polym. Sci.* **2012**, *123*, 2431.
[18] L. Guo, S. Chen, L. Chen, *Colloid. Polym. Sci.* **2007**, *285*, 1593.
[19] L. Chen, C. Wang, Q. Li, S. Yang, L. Hou, S. Chen, *J. Mater. Sci.* **2009**, *44*, 3413.
[20] W.-K. Li, G.-D. Zhou, T. Mak, Eds. Advanced Structural Inorganic Chemistry; Oxford Science Publications: New York, **2008**.
[21] K. Wright, R. A. Jackson, *J. Mater. Chem.* **1995**, *5*, 2037.
[22] H. Zhang, F. Huang, B. Gilbert, J. F. Banfield, *J. Phys. Chem. B* **2003**, *107*, 13051.
[23] H. Zhang, B. Gilbert, F. Huang, J. F. Banfield, *Nature* **2003**, *424*, 1025.
[24] H. Zhang, J. R. Rustad, J. F. Banfield, *J. Phys. Chem. A* **2007**, *111*, 5008.
[25] H. Zhang, J. F. Banfield, *Nano Lett.* **2004**, *4*, 713.
[26] K. Wright, J. D. Gale, *Phys. Rev. B* **2004**, *70*, 035211.
[27] S. Hamad, S. Cristol, C. R. A. Catlow, *J. Phys. Chem. B* **2002**, *106*, 11002.
[28] M. Grünwald, A. Zayak, J. N. Neaton, P. L. Geissler, *J. Chem. Phys.* **2012**, *136*, 234111.
[29] S. Hamad, C. R. A. Catlow, E. Spanó, J. M. Matxain, J. M. Ugalde, *J. Phys. Chem. B* **2005**, *109*, 2703.
[30] S. Hamad, C. R. A. Catlow, *J. Cryst. Growth* **2006**, *294*, 2.
[31] S. Hamad, S. M. Woodley, C. R. A. Catlow, *Mol. Simul.* **2009**, *35*, 1015.
[32] T. A. Halgren, W. Damm, *Curr. Opin. Struct. Biol.* **2001**, *11*, 236.
[33] R. A. Scranton, J. S. Best, J. O. McCaldin, *J. Vac. Sci. Technol.* **1977**, *14*, 930.
[34] B. G. Dick, A. W. Overhauser, *Phys. Rev.* **1958**, *112*, 90.
[35] C. Chen, J. K. Maranas, V. García-Sakai, *Macromolecules* **2006**, *39*, 9630.
[36] J. D. Gale, *J. Chem. Soc., Faraday Trans.* **1997**, *93*, 629.
[37] J. D. Gale, A. L. Rohl, *Mol. Simul.* **2003**, *29*, 291.
[38] E. R. Cope, M. T. Dove, *J. Appl. Crystallogr.* **2007**, *40*, 589.
[39] J. L. Birman, *Phys. Rev.* **1958**, *10*, 810.
[40] E. H. Kisi, M. M. Elocombe, *Acta Cryst.* **1989**, *C45*, 1867.
[41] F. Birch, *Phys. Rev.* **1947**, *71*, 809.
[42] D. Vanderbilt, *Phys. Rev. B* **1990**, *41*, 7892.
[43] D. Marx, J. Hutter, Ab Initio Molecular Dynamics: Basic Theory and Advanced Methods; Cambridge University Press: Cambridge, **2009**.
[44] CPMD, Version 3.12, IBMCorp 1990–2012, MPI für Festkörperforschung Stuttart 1997–2001; IBM Research laboratory, Rüschlikon. Available at: http://www.cpmd.org.
[45] R. W. Hockney, *Methods Comput. Phys.* **1970**, *9*, 136.
[46] The DLPOLY Molecular Simulation Package, 2.20, W. Sumit, T. R. Forester, I. T. Todorov, M. Leslie, STFC Daresbury Laboratory, Daresbury, Warrington, U.K., 1999; Available at: http://www.ccp5.ac.uk/DL_POLY/. Accessed on Sep 24 2013.
[47] M. P. Allen, D. J. Tildesley, Computer Simulation of Liquids; Clarendon Press: Oxford, **1989**.
[48] W. G. Hoover, *Phys. Rev. A* **1985**, *31*, 1695.
[49] R. Car, M. Parrinello, *Phys. Rev. Lett.* **1985**, *55*, 2471.
[50] G. J. Martyna, M. L. Klein, M. Tuckerman, *J. Chem. Phys.* **1992**, *97*, 2635.

[51] O. Modelung, Landolt-Bornstein, Eds. Numerical Data and Functional Relationships in Science and Technology; Springer-Verlag: Berlin, **1982**.
[52] J. E. Jaffe, R. Pandey, M. J. Seel, *Phys. Rev. B* **1993**, *47*, 6299.
[53] A. Qteish, M. Parrinello, *Phys. Rev. B* **2000**, *61*, 6521.
[54] X.-R. Chen, X.-F. Li, L.-C. Cai, J. Zhu, *Solid State Commun.* **2006**, *139*, 246.
[55] R. Gangadharan, V. Jayalakshmi, J. Kalaiselvi, S. Mohan, R. Murugan, B. Palanivel, *J. Alloys Compd.* **2003**, *359*, 22.
[56] M. Catti, Y. Noel, R. Dovesi, *J. Phys. Chem. Solids* **2003**, *64*, 2183.
[57] C.-Y. Yeh, Z. W. Lu, S. Froyen, A. Zunger, *Phys. Rev. B* **1992**, *46*, 10086.
[58] E. Hu Cui, Z.-Y. Zeng, Y. Cheng, X.-R. Chen, L.-C. Cai, *Chin. Phys. B* **2008**, *17*, 3867.
[59] D. Berlincourt, H. Jaffe, L. R. Shiozawa, *Phys. Rev.* **1963**, *129*, 1009.
[60] R. A. Casali, N. E. Christensen, *Solid State Commun.* **1998**, *108*, 793.
[61] T. V. Anil, C. S. Menon, K. S. Krishna Kumar, K. P. Jayachandran, *J. Phys. Chem. Solids* **2004**, *65*, 1053.
[62] J. F. Nye, Physical Properties of Crystals; Oxford University Press, New York, **1957**.
[63] J. L. Martins, N. Troullier, S. H. Wei, *Phys. Rev. B* **1991**, *43*, 2213.

Received: 11 November 2014
Revised: 6 February 2015
Accepted: 11 March 2015
Published online on 21 April 2015